Cluster dynamical mean field theory study of antiferromagnetic transition in the square-lattice Hubbard model: Optical conductivity and electronic structure

Toshihiro Sato[1] and Hirokazu Tsunetsugu[2]

[1]*Computational Condensed Matter Physics Laboratory, RIKEN, Wako, Saitama 351-0198, Japan*

[2]*The Institute for Solid State Physics, The University of Tokyo, Kashiwa, Chiba 277-8581, Japan*

(Received 26 April 2016; revised manuscript received 22 July 2016; published 8 August 2016; corrected 12 August 2016)

We numerically study optical conductivity $\sigma(\omega)$ near the "antiferromagnetic" phase transition in the square-lattice Hubbard model at half filling. We use a cluster dynamical mean field theory and calculate conductivity including vertex corrections and, to this end, we have reformulated the vertex corrections in the antiferromagnetic phase. We find that the vertex corrections change various important details in temperature and ω dependencies of conductivity in the square lattice, and this contrasts sharply the case of the Mott transition in the frustrated triangular lattice. Generally, the vertex corrections enhance variations in the ω dependence, and sharpen the Drude peak and a high-ω incoherent peak in the paramagnetic phase. They also enhance the dip in $\sigma(\omega)$ at $\omega = 0$ in the antiferromagnetic phase. Therefore, the dc conductivity is enhanced in the paramagnetic phase and suppressed in the antiferromagnetic phase, but this change occurs slightly below the transition temperature. We also find a temperature region above the transition temperature in which the dc conductivity shows an insulating behavior but $\sigma(\omega)$ retains the Drude peak, and this region is stabilized by the vertex corrections. We also investigate which fluctuations are important in the vertex corrections and analyze momentum dependence of the vertex function in detail.

DOI: 10.1103/PhysRevB.94.085110

I. INTRODUCTION

Dynamical mean field theory (DMFT) [1] has advanced the investigation of many aspects in strongly correlated electronic systems described by the Hubbard models. This powerful approach is exact on the Bethe lattice with an infinite coordination number and has been very successful in demonstrating the Mott metal-insulator transition induced by electron correlations [1], as well as magnetically ordered states by capturing short-range correlations. Cluster extensions of the DMFT, i.e., dynamical cluster approximation (DCA) [2] and cluster DMFT (CDMFT) [3], which include both on-site and short-range correlations inside the cluster, has made steady progress in our understanding of the Mott transition [4–14]. Examples include the phase diagram in the parameter space of temperature and Coulomb repulsion strength [9,11,12] and thermodynamic criticality of the Mott transition [15–17]. A typical realization of the square-lattice Hubbard model is cuprate superconductors and related materials. Pseudogap state and superconductivity in those systems have been studied actively by using both the DCA [18–20] and CDMFT approaches [21–28]. Another typical realization of the two-dimensional Hubbard model is the organic materials κ-(BEDT-TTF)$_2X$, and this has a triangular lattice structure. The CDMFT calculation has demonstrated a reentrant behavior of the Mott transition in an anisotropic triangular lattice [11], which is consistent with experimental results in some members of this material.

Among studies for advancing our understanding of physical properties in the strongly correlated electronic systems, transport properties are an active topic of research and several experimental results have been reported. As a typical example, optical conductivity provides useful information on charge dynamics, in particular, effective mass and transport scattering process, as well as electric structure. In the previous theoretical works of the DMFT [29–35] and the CDMFT [36–38], optical conductivity of the Hubbard model has been calculated simply by convoluting single-electron Green's functions. These calculations have captured a clear difference in charge dynamics between the metallic and the insulating states. However, to take into account correlation effects further, we need a numerical approach that incorporates nonlocal correlations in conductivity beyond the standard formulation. This has been put forward by including vertex corrections inside the cluster based on the developed cluster extensions by the DCA [38,39]. They were employed only for the paramagnetic phase in a square-lattice system, and the results suggested that the vertex corrections make a significant contribution, in particular at and near half filling. Our previous study also reported the achievement of the vertex correction implementation in the CDMFT for optical conductivity [17], and it focused on the paramagnetic phase in a triangular-lattice system. In this case, the effects of the vertex corrections are not drastic, and this may be attributed to the weak momentum dependence of spin correlations due to frustration in the triangular lattice.

These developments in the two methods are crucial to investigate correlation effects on electronic transport, particularly concerning the Mott transition. However, it is highly desirable to examine the effects of magnetic fluctuation on electronic transport for the case when their divergence drives a phase transition. This is the main issue of this paper and we are going to study optical conductivity near the antiferromagnetic phase transition in a square-lattice Hubbard model at half filling. For this purpose, we develop a numerical method for optical conductivity including vertex corrections in the CDMFT, which includes effects of magnetic fluctuations. We then use this method and investigate the effect of vertex corrections near the antiferromagnetic transition temperature in the square-lattice Hubbard model at half filling. Note that precisely speaking the antiferromagnetic transition does not occur at any finite temperature in an isolated layer of two dimensions, but one should understand that our calculations

mimic a corresponding study on a quasi-two-dimensional system.

This paper is organized as follows. We start in Sec. II describing our model, and then explain a new formulation of vertex corrections in optical conductivity developed for the antiferromagnetic phase. Before showing results of conductivity, we briefly discuss in Sec. III magnetic ordering and change in electronic structure with the ordering. In Sec. IV, we show the results of optical conductivity including the vertex corrections, and then discuss the effects of the vertex corrections on dc conductivity. The effects on ω dependence are discussed in detail in Sec. V, and we also analyze which type of fluctuations are important. In Sec. VI, we analyze momentum dependence of the vertex function and investigate how the dependence changes with temperature. Section VII concludes this paper with an extended summary.

II. MODEL AND METHOD

The model we consider in this paper is a single-band Hubbard Hamiltonian on a square lattice at half filling,

$$H = -t \sum_{\langle i,j\rangle,\sigma} c^{\dagger}_{i\sigma} c_{j\sigma} + U \sum_{i} n_{i\uparrow} n_{i\downarrow} - \mu \sum_{i,\sigma} c^{\dagger}_{i\sigma} c_{i\sigma}. \quad (1)$$

Here, t is the nearest-neighbor hopping amplitude, and U is the on-site Coulomb repulsion. The chemical potential μ is set to $U/2$ to tune the electron density at half filling $\langle n_{i\uparrow} + n_{i\downarrow}\rangle = 1$. $c_{i\sigma}$ is the electron annihilation operator at site i with spin $\sigma = \uparrow,\downarrow$, and $n_{i\sigma} \equiv c^{\dagger}_{i\sigma} c_{i\sigma}$. The kinetic energy of the electron with the momentum $\mathbf{k}$ is $\epsilon_{\mathbf{k}} = -2t(\cos k_x + \cos k_y)$. Throughout this paper, the energy unit is $t = 1$ and U and T are measured in this unit, and all the data are calculated for $U = 6.5$.

To take into account both strong short-range electronic correlations and magnetic fluctuations, we use the cluster dynamical mean field theory (CDMFT) [3] employing a four-site square cluster. We compute the single- and two-electron Green's functions inside this cluster by using the continuous-time quantum Monte Carlo (CTQMC) method based on the strong coupling expansion [40] for a given effective medium. The effective medium $\hat{\mathcal{G}}_{\sigma}(\tau)$ and the cluster signle-electron Green's function $\hat{G}_{\sigma}(\tau)$ are both a 4×4 matrix in the cluster, and quantities with $\hat{}$ symbol denote 4×4 matrices in the following. Its element is defined for imaginary time τ as $G^{ij}_{\sigma}(\tau) = -T_{\tau}\langle c_{i\sigma}(\tau) c^{\dagger}_{j\sigma}(0)\rangle$, where i and j are the sites in the cluster and the imaginary-time operator is defined as [41] $c_{i\sigma}(\tau) \equiv e^{\tau H} c_{i\sigma} e^{-\tau H}$. T_{τ} is the time-ordering operator and $\langle \cdots \rangle$ denotes the thermal average. After the effective medium $\hat{\mathcal{G}}_{\sigma}(i\omega_n)$ is self-consistently determined in the Matsubara-frequency space, we determine the cluster self-energy via the Dyson equation $\hat{\Sigma}_{\sigma}(i\omega_n) = \hat{\mathcal{G}}^{-1}_{\sigma}(i\omega_n) - \hat{G}^{-1}_{\sigma}(i\omega_n)$.

In this paper, we show the results solely for $U = 6.5$. This choice is close to the value at the critical end point of the line of the first-order Mott metal-insulator transition in the U-T phase diagram determined by CDMFT approaches under the condition that no magnetic transitions occur [9]. Since the square lattice is bipartite, the ground state at half filling electron density has an antiferromagnetic order for any $U > 0$. The calculation by Kent *et al.* showed that the antiferromagnetic transition temperature is highest at $U/(12t) \sim 10/12 = 0.83$ in the three-dimensional cubic lattice [42], where $12t$ is the bandwidth. In the square lattice, the bandwidth is $8t$ and this ratio corresponds to $U/t \sim 0.83 \times 8 \sim 6.7$. As this is close to our choice, we may expect a high transition temperature, and this is an advantage in numerical computation. However, we should note that this finite-temperature transition is an artifact of the use of the CDMFT, as Mermin-Wagner theorem [43] proves its absence in two dimensional lattices. Thus our results for the square lattice should be understood as for a corresponding quasi-two-dimensional model, in which the magnetic order is stabilized by interlayer couplings but other physical properties are essentially determined in each layer. Despite this limitation, the CDMFT approach can take into account important short-range quantum and thermal fluctuations in our investigation of conductivity near a real antiferromagnetic transition.

In our CDMFT calculations, we calculate the single-particle spectrum $A_{\mathbf{k}\sigma}(\omega)$ for electron with the wave vector $\mathbf{k}$ and spin σ. The dependence on the real frequency ω is obtained by the maximum entropy method (MEM) [44] from the Monte Carlo data for imaginary time.

In the antiferromagnetic phase, we choose the spin axis such that local magnetizations point to $\pm z$ direction. The order parameter is the staggered magnetization defined by $m^{(a)}_{z} = \frac{1}{N}\sum_{i\in a}\sum_{\sigma}\sigma\langle n_{i\sigma}\rangle$, where the spin is counted as $\sigma = 1(-1)$ for $\uparrow$ ($\downarrow$), and $a = A, B$ being the sublattice index. N is the total number of sites. The relation $m^{(B)}_{z} = -m^{(A)}_{z}$ holds exactly in the square lattice, since the combination of spin inversion and lattice translation by (1,0) remains a symmetry operation. Because the two sublattices are not equivalent, the Brillouin zone halves as shown in Fig. 1(c). Correspondingly, for labeling electron, one needs an additional sublattice index as well as the momentum $(a,\mathbf{p})$ in the reduced half Brillouin zone:

$$c_{A\mathbf{p}} = \frac{c_{\mathbf{p}} + c_{\mathbf{p}+\mathbf{Q}}}{\sqrt{2}}, \quad c_{B\mathbf{p}} = \frac{c_{\mathbf{p}} - c_{\mathbf{p}+\mathbf{Q}}}{\sqrt{2}}, \quad (2)$$

where $\mathbf{Q} = (\pi,\pi)$ and the spin index is omitted. Each electron propagates from one sublattice to the other, and therefore the single-electron Green's function G is now a 2×2 matrix in the sublattice space. Its element is defined as $G^{ab}_{\mathbf{p}\sigma}(\tau) = -T_{\tau}\langle c_{a\mathbf{p}\sigma}(\tau) c^{\dagger}_{b\mathbf{p}\sigma}(0)\rangle$, where $c_{a\mathbf{p}\sigma}(\tau)$ is defined for the imaginary time τ as before. While the momentum $\mathbf{p}$ is trivially conserved, spin projection σ conserves because of the remaining spin rotation symmetry about the direction of the staggered magnetization.

In two dimensions, optical conductivity $\sigma_{\alpha\alpha'}(\omega)$ is a 2×2 matrix, and the linear response theory [45] shows that it is defined by the current correlation function $\chi_{\alpha\alpha'}(\mathbf{q},\omega)$ in the limit of the wave vector $\mathbf{q} \to \mathbf{0}$. Its real part is given in the unit of quantum conductance $(e^2/\hbar)$ as

$$\sigma_{\alpha\alpha'}(\omega) = \mathrm{Re}\,\frac{\chi_{\alpha\alpha'}(\mathbf{0},\omega) - \chi_{\alpha\alpha'}(\mathbf{0},0)}{i\omega}, \quad (3)$$

where Re denotes the real part and $\alpha,\alpha' \in \{x,y\}$ are the directions of current and electric field, respectively. Note also that $\chi_{\alpha\alpha'}(\mathbf{0},\omega)$ is obtained from the correlation function of uniform particle currents $\{J_{\alpha}\}$ [see Eq. (7)] in imaginary time, $\chi_{\alpha\alpha'}(\mathbf{0},\tau) = -T_{\tau}\langle J_{\alpha}(\tau) J_{\alpha'}(0)\rangle$, where $J_{\alpha}(\tau)$ is also defined as before for the imaginary time τ. Its Fourier transform is

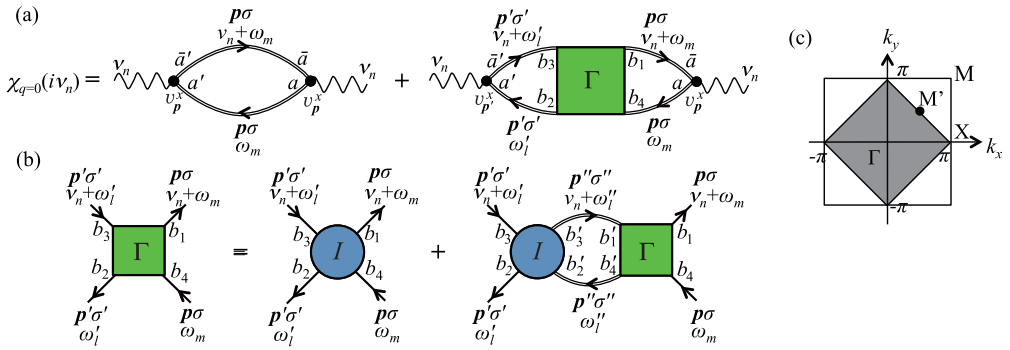

FIG. 1. Feynman diagrams in the antiferromagnetic phase for (a) current correlation function $\chi(i\nu_n)$ in Eqs. (4)–(6) and (b) full vertex function $\Gamma^{b_4b_1b_2b_3}_{\mathbf{p}\sigma\mathbf{p}'\sigma'}(i\nu_n)$ in Eq. (8). Results for the paramagnetic phase are obtained by omitting the sublattice indices and changing the momentum sums to over the original Brillouin zone. (c) Brillouin zone of the square lattice. Gray zone is the reduced Brillouin zone in the antiferromagnetic phase.

a function of bosonic Matsubara frequency $i\nu_n = 2ni\pi T$, and the real-frequency correlation function is obtained by the analytic continuation, $\chi_{\alpha\alpha'}(\mathbf{0},\omega) = \chi_{\alpha\alpha'}(\mathbf{0},i\nu_n)|_{i\nu_n\to\omega+i0}$. In numerical calculation, we perform the analytic continuation by using the MEM [44]. In our case, the conductivity has only an isotropic part, since the antiferromagnetic order keeps the lattice rotation symmetry about each site, and therefore $\sigma_{\alpha\alpha'}(\omega) = \sigma(\omega)\delta_{\alpha\alpha'}$ and $\chi_{\alpha\alpha'}(\mathbf{0},\omega) = \chi(\mathbf{0},\omega)\delta_{\alpha\alpha'}$ not only in the paramagnetic phase but also in the antiferromagnetic phase.

To take into account correlation effects, we have included vertex corrections in CDMFT in the calculation of $\sigma(\omega)$ and reported the results in the paramagnetic phase of the frustrated Hubbard model [17]. However, in the antiferromagnetic phase, the Brillouin zone halves and this requires the reformulation of the vertex corrections, which has not been achieved yet. In this paper, we derive this reformulation and investigate the effects of magnetic instability on transport properties.

Modifying our previous formulation of the vertex corrections, we have derived for the antiferromagnetic phase a formula with taking account of the new sublattice degrees of freedom. The current correlation function is now obtained in Matsubara space as [46]

$$\chi(i\nu_n) = \chi_0(i\nu_n) + \chi_{\rm vc}(i\nu_n), \tag{4}$$

$$\chi_0(i\nu_n) = \sum \left(v^x_{\mathbf{p}}\right)^2 K^{\bar{a}aa'\bar{a}'}_{\mathbf{p}\sigma}(i\nu_n; i\omega_m), \tag{5}$$

$$\chi_{\rm vc}(i\nu_n) = \sum\sum{}' v^x_{\mathbf{p}} v^x_{\mathbf{p}'}\, K^{\bar{a}ab_4b_1}_{\mathbf{p}\sigma}(i\nu_n; i\omega'_l) \times \Gamma^{b_4b_1b_2b_3}_{\mathbf{p}\sigma\mathbf{p}'\sigma'}(i\nu_n)\, K^{b_2b_3a'\bar{a}'}_{\mathbf{p}'\sigma'}(i\nu_n; i\omega_m), \tag{6}$$

and the vertex correction $\chi_{\rm vc}$ is represented with the vertex function Γ. Here, $v^x_{\mathbf{p}} = \frac{\partial}{\partial p_x}\epsilon_{\mathbf{p}} = 2\sin p_x$ is the x component of current, and $\sum$ and $\sum'$ are $\frac{T}{N}\sum_{\mathbf{p}\sigma}\sum_{\omega_m}\sum_{a,a'}$ and $\frac{T}{N}\sum_{\mathbf{p}'\sigma'}\sum_{\omega'_l}\sum_{\{b\}}$, respectively. K is a product of two single-electron Green's functions shown by double lines, $K^{baa'b'}_{\mathbf{p}\sigma}(i\nu_n; i\omega_m) = G^{a'a}_{\mathbf{p}\sigma}(i\omega_m)G^{bb'}_{\mathbf{p}\sigma}(i\nu_n + i\omega_m)$. It is important to note that the bare current vertices shown by black circles in Fig. 1(a) have a special symmetry in the sublattice space. Two sublattice indices at each bare vertex should be opposite (a and $\bar{a}$, etc.) and this is because electrons hop only between different sublattices in the model (1). We can also show this directly by representing current with the new operators,

$$J_\alpha = \sum_{\mathbf{k}}^{\text{full BZ}}\sum_{\sigma} v^\alpha_{\mathbf{k}} c^\dagger_{\mathbf{k}\sigma} c_{\mathbf{k}\sigma} = \sum_{\mathbf{p}}^{1/2\text{ BZ}}\sum_{a\sigma} v^\alpha_{\mathbf{p}} c^\dagger_{a\mathbf{p}\sigma} c_{\bar{a}\mathbf{p}\sigma}, \tag{7}$$

where the relation $v^\alpha_{\mathbf{p}+\mathbf{Q}} = -v^\alpha_{\mathbf{p}}$ is used. As depicted in Fig. 1(a), χ_0 corresponds to the bubble diagram [the first part on the right hand side (RHS)], and calculated from K. Note that these single-electron Green's functions include the self energy calculated in the CDMFT. We directly calculate the single- and two-electron Green's functions within the cluster as a function of imaginary time τ by the CTQMC solver.

For calculating the lattice Green's function, we employ the cumulant periodization method [22] in this CDMFT study. It is known that this method works well in a wide range of weak to strong Coulomb repulsion [22]. In this method, we first introduce the cluster cumulant, $\hat{M}_\sigma(i\omega_n) = [(i\omega_n + \mu)\hat{\mathbf{1}} - \hat{\Sigma}_\sigma(i\omega_n)]^{-1}$, where $\hat{\Sigma}_\sigma(i\omega_n)$ is the cluster self-energy and quantities with $\hat{}$ symbol are 4×4 matrices in the cluster. In the paramagnetic case, the cumulant does not depend on spin, $\hat{M}_\sigma = \hat{M}$, and we proceed to calculate the lattice cumulant for the momentum $\mathbf{k}$ in the original Brillouin zone as $M_{\mathbf{k}}(i\omega_n) = \frac{1}{4}\sum_{i,j} M^{ij}(i\omega_n)e^{-i\mathbf{k}\cdot(\mathbf{r}_i-\mathbf{r}_j)}$, where the sum $\sum_{i,j}$ is taken over all the site pairs inside the cluster. From this periodization, we calculate the lattice Green's function as $G_{\mathbf{k}\sigma}(i\omega_n) = [M_{\mathbf{k}}(i\omega_n)^{-1} - \epsilon_{\mathbf{k}}]^{-1}$.

In the antiferromagnetic case, the cluster Green's function is still a 4×4 matrix with respect to site indices and diagonal in spin space, but this now depends on spin leading to $\hat{M}_\uparrow \neq \hat{M}_\downarrow$. The lattice Green's function is diagonal in spin space but a 2×2 matrix in the sublattice space, $\underline{G}_{\mathbf{p}\sigma} = \{G^{ab}_{\mathbf{p}\sigma}\}$, where $\mathbf{p}$ is limited to inside the reduced Brillouin zone. In what follows, quantities with the $\underline{\ }$ symbol denote 2×2 matrices in the sublattice space. The lattice cumulant also has the same symmetry, and its element is calculated as $[\underline{M}_{\mathbf{p}\sigma}(i\omega_n)]^{ab} = \frac{1}{2}\sum_{i\in a}\sum_{j\in b} M^{ij}_\sigma(i\omega_n)e^{-i\mathbf{p}\cdot(\mathbf{r}_i-\mathbf{r}_j)}$, where the sums $\sum_i$ and $\sum_j$ are taken over the sites belonging to each sublattice inside the cluster. Finally, the lattice Green's function is obtained as $\underline{G}_{\mathbf{p}\sigma}(i\omega_n) = [\underline{M}_{\mathbf{p}\sigma}(i\omega_n)^{-1} - \underline{\epsilon}_{\mathbf{p}}]^{-1}$, where $\underline{\epsilon}$ is the Fourier-transformed hopping matrix, $[\underline{\epsilon}_{\mathbf{p}}]^{ab} = (1-\delta_{ab})\epsilon_{\mathbf{p}}$. Within our knowledge, this is an achievement of

the cumulant periodization for the lattice Green's function in the antiferromagnetic case.

Our formulation shown in Eq. (6) and Fig. 1(a) uses the approximation for the vertex function Γ such that its dependence on internal frequencies ω_l and ω'_m is averaged over. Some previous studies investigated the vertex correction to the spin susceptibility in the single-site DMFT approach and compared the full vertex correction and the approximated result averaged over two internal frequencies. They have reported that this approximation well reproduces the spin susceptibility calculated with the full vertex function qualitatively [47,48]. Calculation of the full vertex function in the cluster DMFT is impractical even with the present computer resources. We use this approximation in this study, but this is an important future problem to be checked.

Calculation of the vertex function Γ takes a few steps. By using the CTQMC method, we first calculate directly two-electron Green's functions inside the cluster [41] $\mathcal{K}^{\sigma\sigma'}_{iji'j'}(\tau) \equiv \langle c^\dagger_{i\sigma}(\tau) c_{j\sigma}(\tau) c^\dagger_{i'\sigma'}(0) c_{j'\sigma'}(0)\rangle$, where the four sites i–j' are all in the cluster. We then evaluate the irreducible vertex function in the cluster $I^{\sigma\sigma'}_{iji'j'}(i\nu_n)$ by solving the Bethe-Salpeter equation $\mathcal{K}^{\sigma\sigma'}_{iji'j'}(i\nu_n) = K^{\sigma\sigma'}_{iji'j'}(i\nu_n) + \sum_{nm,n'm'} \sum_{\sigma''\sigma'''} \mathcal{K}^{\sigma\sigma''}_{ijnm}(i\nu_n)\, I^{\sigma''\sigma'''}_{nmn'm'}(i\nu_n)\, K^{\sigma'''\sigma'}_{n'm'i'j'}(i\nu_n)$, where K denotes the contribution of a product of two single-electron Green's functions. The lattice irreducible vertex is then obtained as its Fourier component $I^{b_4b_1b_2b_3}_{\mathbf{p}\sigma\mathbf{p}'\sigma'}(i\nu_n) = \sum_{ij,i'j'} I^{\sigma\sigma'}_{ij,i'j'}(i\nu_n)\, e^{i\mathbf{p}\cdot(\mathbf{r}_i-\mathbf{r}_j)+i\mathbf{p}'\cdot(\mathbf{r}_{i'}-\mathbf{r}_{j'})}$, where the sum is taken over all the combinations under the condition that the sites i, j, i', j' are in the sublattice b_4, b_1, b_2, and b_3, respectively. Once I is obtained, the lattice reducible vertex Γ is calculated by solving the Bethe-Salpeter equation that is diagrammatically shown in Fig. 1(b),

$$\Gamma^{b_4b_1b_2b_3}_{\mathbf{p}\sigma\mathbf{p}'\sigma'}(i\nu_n) = I^{b_4b_1b_2b_3}_{\mathbf{p}\sigma\mathbf{p}'\sigma'}(i\nu_n) + \sum \Gamma^{b_4b_1b'_4b'_1}_{\mathbf{p}\sigma\mathbf{p}''\sigma''}(i\nu_n) \times K^{b'_4b'_1b'_2b'_3}_{\mathbf{p}''\sigma''}(i\nu_n; i\omega''_l)\, I^{b'_2b'_3b_2b_3}_{\mathbf{p}''\sigma''\mathbf{p}'\sigma'}(i\nu_n). \quad (8)$$

Here, $\sum$ is a shorthand for $\frac{T}{N}\sum_{\mathbf{p}''\sigma''}\sum_{\omega''_l}\sum_{\{b'\}}$. The current correlation in Matsubara space $\chi(i\nu_n)$ is obtained from Eq. (6) with this Γ. Finally, we calculate the real part of conductivity $\sigma(\omega)$ by analytic continuation $i\nu_n \to \omega + i0$ by using the MEM [44]. We note that this new algorithm reproduces our previous formula derived for the paramagnetic case [17] by omitting the sublattice indices and taking wave vector $\mathbf{p}$ in the original Brillouin zone as shown in Fig. 1(c).

Here we make a note for our formulation regarding spin order. The result of current correlation function, Eqs. (4)–(6), is formulated for the Néel-type antiferromagnetic order, and in this case the current correlation is isotropic in space, $\chi_{\alpha\alpha'} = \chi\delta_{\alpha\alpha'}$. This isotropy originates from the lattice rotation symmetry and it is not limited to the Néel order. For example, any spin order with a two-site magnetic unit cell has the $\pi/2$-rotation symmetry. Therefore, the current correlation remains isotropic, but we need to generalize Eqs. (5) and (6) if spin order is noncollinear. The single-electron Green's function is no longer diagonal in spin space and has finite off-diagonal elements $G_{\uparrow\downarrow}$ and $G_{\downarrow\uparrow}$. Correspondingly, K and Γ need four spin indices, and one needs their full contraction in Eq. (6), but the spin index should be diagonal at the bare current vertices shown by dots in Fig. 1.

Calculation of two-electron Green's functions is a big challenge in numerical computations due to their huge complexity. $K^{\sigma\sigma'}_{iji'j'}(\tau)$ has $4^4 \times 2^2 = 1024$ combinations of four site indices plus two spin indices, and we directly sample all of them in our CTQMC calculations. Therefore, even after very long MC runs, only a limited number of MC samples are collected for each element. Therefore, it is important to reduce statistical errors in K, and we use two techniques for this purpose. First, using the point group symmetry augmented with the spin inversion operation, we average over equivalent elements of $K^{\sigma\sigma'}_{iji'j'}$ to enforce the correct symmetry. Secondly, we eliminate noise in the τ dependence using a high-cut filter. We know the large-ν_n asymptotic form of the Fourier components $K(i\nu_n)$ owing to its spectral representation, and we fit our data to its form. With these two techniques, we improve accuracy of the two-electron Green's functions and proceed with thus obtained reliable data to the next steps of calculation. For example, for $T = 0.30$, we typically carry out about 10^9 MC sweeps in each sample and average over 1024 samples. The error of the current correlation is, for example, $\Delta\chi/\chi \sim 0.03$ at $\tau = 0$.

We also make a comment that this new algorithm for the vertex correction in conductivity can be easily generalized for other response functions like Raman spectrum [49–51], $\chi_R(\tau) = -T_\tau\langle\tilde{\rho}(\tau)\tilde{\rho}(0)\rangle$. The only difference is that one replaces the particle current J_α by a corresponding operator for Raman spectrum, and that is

$$\tilde{\rho} = \sum_{\mathbf{k}\sigma} \gamma_{\mathbf{k}} c^\dagger_{\mathbf{k}\sigma} c_{\mathbf{k}\sigma}, \quad \gamma_{\mathbf{k}} = (\mathbf{e}^I \cdot \nabla_{\mathbf{k}})(\mathbf{e}^S \cdot \nabla_{\mathbf{k}})\epsilon_{\mathbf{k}}, \quad (9)$$

where and $\mathbf{e}^I$ and $\mathbf{e}^S$ are polarization vectors of incident and scattered light, respectively. For the kinetic energy $\epsilon_{\mathbf{k}} = -2(\cos k_x + \cos k_y)$ in our model, the bare vertex also has the symmetry $\gamma_{\mathbf{p}} = -\gamma_{\mathbf{p}+\mathbf{Q}}$, and thus in the antiferromagnetic phase $\tilde{\rho} = \sum_{\mathbf{p}}^{1/2BZ} \sum_{\sigma a} \gamma_{\mathbf{p}} c^\dagger_{a\mathbf{k}\sigma} c_{\bar{a}\mathbf{k}\sigma}$. As for the bare vertex, for example, the B_{1g} Raman mode corresponds to $\mathbf{e}^I = (1,1)/\sqrt{2}$ and $\mathbf{e}^S = (1,-1)/\sqrt{2}$, and therefore $\gamma_{\mathbf{k}} = \cos k_x - \cos k_y = -\gamma_{\mathbf{k}+\mathbf{Q}}$. For the B_{2g} mode, $\mathbf{e}^I = (1,0)$ and $\mathbf{e}^S = (0,1)$ lead to $\gamma_{\mathbf{k}} = 0$ and therefore the B_{2g} mode is Raman inactive.

III. MAGNETIC ORDER AND ELECTRONIC PROPERTIES

Before discussing conductivity, let us examine in this section magnetic order and the variation of electronic state with temperature. Figure 2 shows the T dependence of the staggered magnetization $m_z(T)$. At low temperatures below $T_N \sim 0.34$, antiferromagnetic order appears and the temperature dependence of m_z is well described by the mean-field critical exponent of the order parameter $\beta = 1/2$. This is consistent with the fact that the CDMFT approach is a variant of the mean field approximation.

Figure 3(a) shows the local spectrum of single particle excitations in the A sublattice [52]. In the paramagnetic phase, it coincides with the result in the B sublattice, and it is given by averaging the $\mathbf{k}$-dependent single-particle spectrum in the whole Brillouin zone, $A^{(A)}_\sigma(\omega) = (1/N)\sum_{\mathbf{k}} A_{\mathbf{k}\sigma}(\omega)$, with $A_{\mathbf{k}\sigma}(\omega) = -\frac{1}{\pi}\mathrm{Im}\, G_{\mathbf{k}\sigma}(\omega + i0)$.

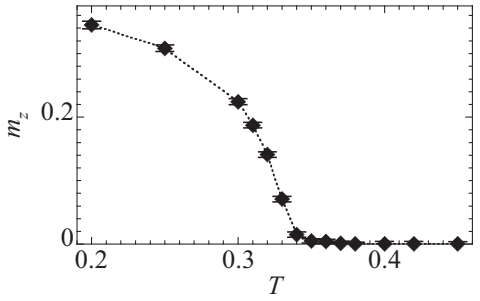

FIG. 2. Temperature dependence on staggered magnetization at $U = 6.5$.

In the antiferromagnetic phase, the Green's functions contain a spin-dependent component and the symmetry of simultaneous spin inversion and sublattice exchange leads to the following property:

$$G^{AA}_{\mathbf{p}\sigma}(i\omega_m) = G^{BB}_{\mathbf{p}\bar{\sigma}}(i\omega_m) = g_{\mathbf{p}}(i\omega_m) + \sigma\Delta_{\mathbf{p}}(i\omega_m),$$
$$G^{a\bar{a}}_{\mathbf{p}\sigma}(i\omega_m) = G^{a\bar{a}}_{\mathbf{p}\bar{\sigma}}(i\omega_m) = \tilde{g}_{\mathbf{p}}(i\omega_m). \quad (10)$$

Δ is the spin-dependent component that appears only in the antiferromagnetic phase. Note that different spin components do not mix, even in the antiferromagnetic phase and these Green's functions are diagonal in the spin space, $G^{ab}_{\mathbf{p}\uparrow\downarrow} = G^{ab}_{\mathbf{p}\downarrow\uparrow} = 0$, since the numbers of up-spin electrons and down-spin electrons are separately conserved in the Néel order. Due to the sublattice dependencies in Eq. (10), the local spectrum differs between the two sublattices, and the value in the a-sublattice is given by $A^{(a)}_{\sigma}(\omega) = -\frac{1}{\pi N}\mathrm{Im}\sum_{\mathbf{p}} G^{aa}_{\mathbf{p}\sigma}(\omega + i0)$. The Green's function $G_{\mathbf{k}}$ is now replaced by $G^{aa}_{\mathbf{p}}$ and the momentum sum is limited to the reduced Brillouin zone. In order to minimize numerical error in $A_{\sigma}(\omega)$, we first took $\mathbf{p}$ summation of the imaginary-time Green's function and then carried out a transformation to real frequency.

Variation with T in the local excitation spectrum reproduces a known behavior for antiferromagnetic transition in the Hubbard model. The spectrum is symmetric in energy, $A_{\sigma}(-\omega) = A_{\sigma}(\omega)$, in the paramagnetic phase, and this comes from the particle-hole symmetry due to the bipartite lattice structure and the half filling electron density. The spectrum shows three peaks, and this is common in the metallic phase of the Hubbard model with large U. The central peak corresponds to quasiparticle excitations, while broad peaks on both sides are the upper and lower Hubbard bands [53]. The central peak sharpens with decreasing temperature above T_N, implying that quasiparticle motion becomes more coherent and the system is metallic. We find that there is no indication of pseudogap formation and the peak evolution is monotonic down to T_N. In the antiferromagnetic phase below T_N, the excitation spectrum splits for different spins, but preserves a generalized particle-hole symmetry, $A^{(a)}_{\sigma}(\omega) = A^{(a)}_{\bar{\sigma}}(-\omega) = A^{(\bar{a})}_{\sigma}(-\omega)$. This is because the antiferromagnetic ordered state remains invariant with respect to the combination of time-reversal operation and exchange of the two sublattices. Below T_N, the spectrum has a dip at $\omega = 0$, and this deepens with lowering T. This manifests that the antiferromagnetic phase is insulating.

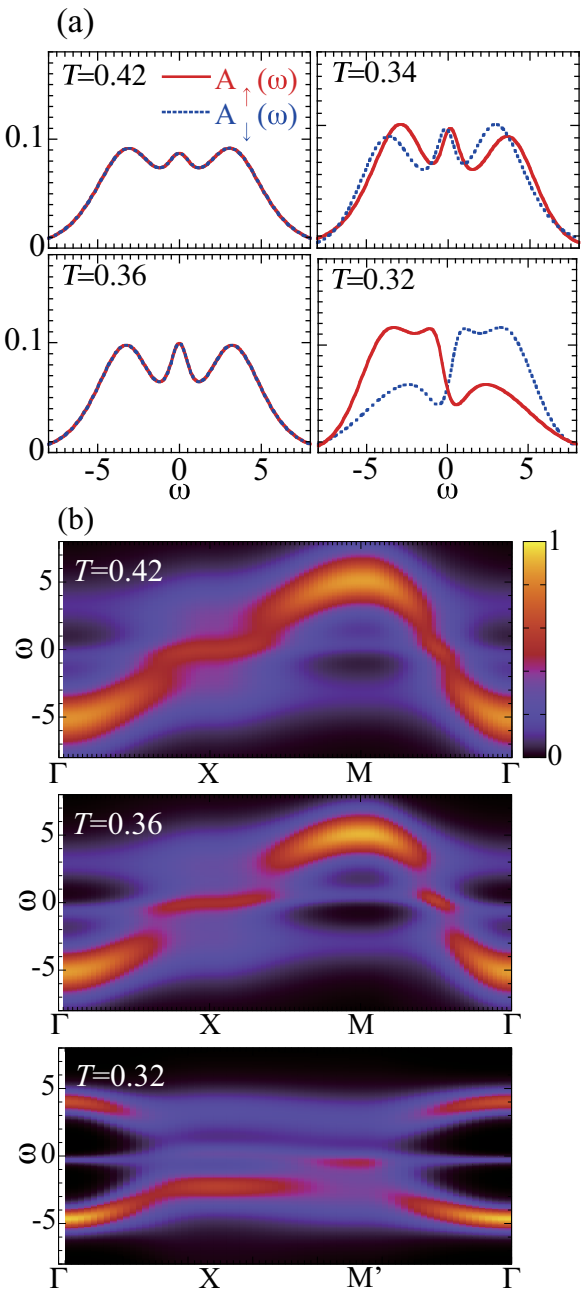

FIG. 3. (a) Local excitations spectrum in the A sublattice $A^{A}_{\sigma}(\omega)$ at four different T's. Note that the spectra for different spins are degenerate at $T = 0.42$ and 0.36. (b) $\mathbf{k}$-resolved single-particle spectral function $A^{A}_{\mathbf{k}\uparrow}(\omega)$ for three different T's along the path for metallic state and insulating state, Γ-X-M-Γ and Γ-X-M'-Γ, respectively in Fig. 1(c). The maximum of each spectral function is normalized to be one.

We discuss the change in electronic structure in more detail by examining the momentum resolved single-particle spectrum. Figure 3(b) presents $A_{\mathbf{k}\sigma}(\omega)$ at three values of T. Figure 1(c) shows color mapping of the spectrum in the paramagnetic and antiferromagnetic phases along the path Γ-X-M-Γ and Γ-X-M'-Γ in the Brillouin zone, respectively. We only present $A_{\mathbf{k}\uparrow}(\omega)$ because of $A_{\mathbf{k}\uparrow}(\omega) = A_{\mathbf{k}\downarrow}(\omega)$ in the paramagnetic state and $A_{\mathbf{k}\uparrow}(\omega) = A_{\mathbf{k}\downarrow}(-\omega)$ in the

antiferromagnetic state. At higher temperature $T = 0.42$, in addition to broad peaks corresponding to the upper and lower Hubbard bands, there exists near $\omega = 0$ a quasiparticle peak. With decreasing T, the energy dispersion of quasiparticle is strongly renormalized to a very flat band, implying the strong correlation effects. At lower temperature $T = 0.32$, this is in the antiferromagnetic phase and the low-energy part of the quasiparticle band disappears, and an excitation gap opens. This is due to scatterings by static staggered moment. In addition, $A_{\mathbf{k}\sigma}(\omega)$ now exhibits a characteristic peak structure near the Fermi energy, which exists near M' point in the Brillouin zone.

IV. OPTICAL/DC CONDUCTIVITY AND EFFECT OF VERTEX CORRECTION

Now, we start with investigating optical conductivity $\sigma(\omega)$ and its dc value. A main issue is its variation with temperature and the effect of vertex corrections. In this section, we are going to investigate characteristics in the T and ω dependence of optical conductivity, while examining the vertex corrections in the next section.

Figure 4(a) shows optical conductivity before including vertex corrections, $\sigma_0(\omega)$. They are calculated from χ_0 in Eq. (5) at various temperatures both above and below T_N. The data including the vertex corrections are plotted in Fig. 4(b). First of all, the vertex corrections are noticeable and they are large particularly at low temperatures. In our previous result for the frustrated Hubbard model on a triangular lattice [17], the difference between $\sigma(\omega)$ and $\sigma_0(\omega)$ is quite small. Therefore, it is remarkable that the vertex corrections are much larger in this unfrustrated system, and the corrections are large already in the paramagnetic phase.

One of the most important characteristics is the dc conductivity, $\sigma_{\rm dc} = \sigma(\omega = 0)$, and this is plotted in Fig. 4(c) as a function of temperature. Values with and without the vertex corrections are denoted as $\sigma_{\rm dc}$ and $\sigma_{0,\rm dc}$, respectively. Before investigating ω dependence, we discuss the dc conductivity and the effects of the vertex corrections on it. When the vertex corrections are not included, $\sigma_{0,\rm dc}$ increases with lowering T in the paramagnetic phase, while it decreases in the antiferromagnetic phase. We find that the dc conductivity shows that the metallic state is smoothly connected to the insulating state with varying T. $\sigma_{0,\rm dc}$ is maximum around $T \sim 0.38$, which is higher than T_N. The data in Fig. 4(c) show that the vertex corrections provide opposite contributions to $\sigma_{\rm dc}$ depending on T. At high temperatures $T \geqslant 0.33$, which is only slightly below $T_N \sim 0.34$, the correction enlarges the dc conductivity. However, the sharp crossover around T_N is enhanced to a steeper slope and $\sigma_{\rm dc}$ is suppressed by the vertex corrections in the low-temperature region. It is noticeable that the $\sigma_{\rm dc}$ maximum shifts to a higher temperature $T \sim 0.40$.

We now examine the ω dependence of $\sigma(\omega)$. A very common feature in all the curves in Figs. 4(a) and 4(b) is a broad peak located around $\omega \sim U$, and this comes from excitations to the upper and lower Hubbard bands [53]. At higher temperatures $T > 0.34$, $\sigma(\omega)$ shows a Drude peak around $\omega = 0$. The system is metallic in this temperature region, and the Drude peak comes from motion of quasiparticles. The peak is not very sharp but its width gradually

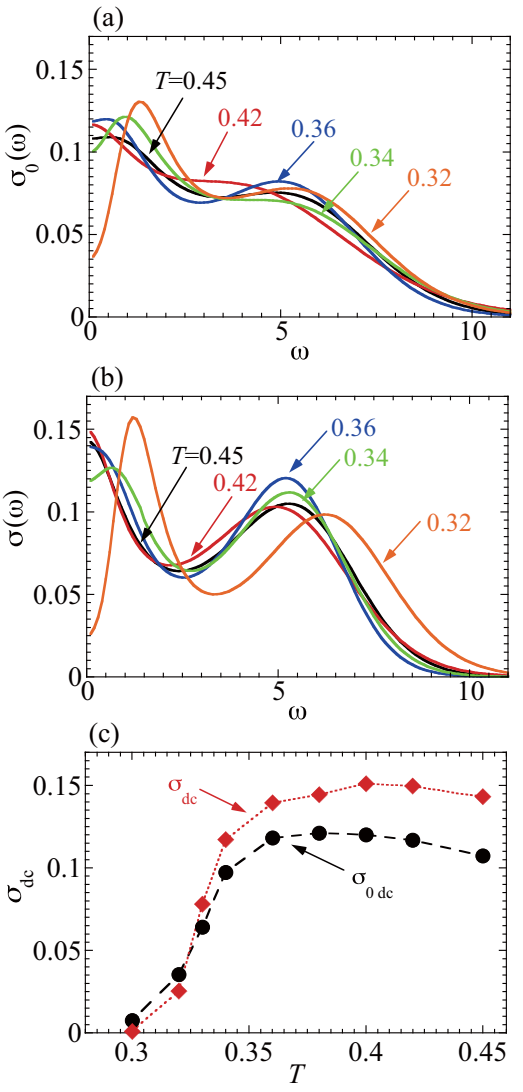

FIG. 4. Optical conductivity (a) without vertex corrections $\sigma_0(\omega)$ and (b) with vertex corrections $\sigma(\omega)$ for various T's. (c) Temperature dependence of dc conductivity with and without vertex corrections.

narrows with decreasing T, while its amplitude increases, which implies enhancement of coherence in quasiparticle motion. The behavior changes below T_N.

With approaching T_N, the Drude peak reduces and this is attributed to enhanced magnetic fluctuations. At $T = 0.34$, the peak that was located around $\omega = 0$ now shifts to a finite energy $\omega \sim 1$, and there appears a dip at $\omega = 0$, which is a characteristic of the insulating phase. This comes from the gap opening in the electron spectrum discussed for the data in Fig. 3. With further decreasing temperature down to $T = 0.32$, the peak shifts towards higher ω and its intensity grows. Correspondingly, the dip at $\omega = 0$ deepens. As discussed in the previous section, quasiparticle bands open a gap in the antiferromagnetic phase. The low-energy peak around $\omega \sim 1$ comes from these quasiparticles in the gapped bands.

V. DETAILED ANALYSIS OF VERTEX CORRECTION

The vertex corrections in the dc conductivity were studied in the previous section, and we now proceed to examine their

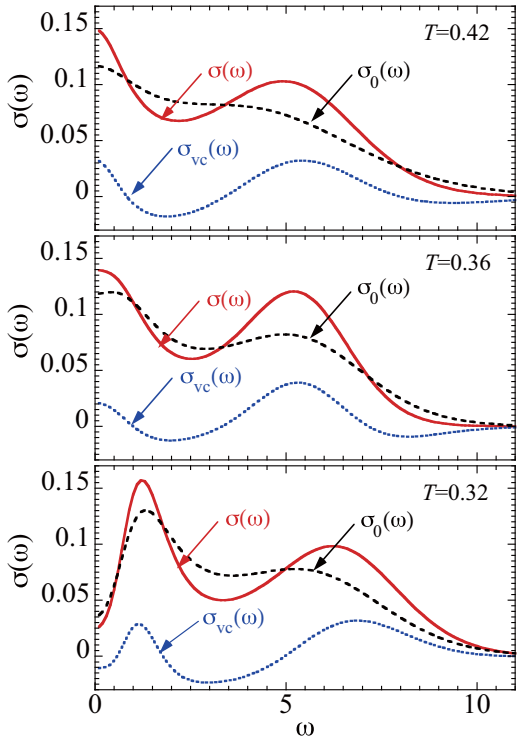

FIG. 5. Effects of vertex corrections on optical conductivity $\sigma(\omega)$ in the paramagnetic phase ($T = 0.42, 0.36$) and the antiferromagnetic phase ($T = 0.32$). $\sigma = \sigma_0 + \sigma_{\rm vc}$.

effects on the ω dependence of the optical conductivity, by analyzing the data in Fig. 4. Detailed comparison is presented in Fig. 5 for three T values, where $\sigma(\omega)$ and $\sigma_0(\omega)$ are the result with and without the vertex corrections, respectively. $\sigma_{\rm vc}(\omega)$ is the vertex correction calculated from $\chi_{\rm vc}$. General features in their dependence on ω and T are similar to each other, but the vertex corrections provide quite pronounced differences in the detailed ω dependence. Like in the case of $\sigma_{\rm dc}(T)$, it is interesting that the vertex corrections behave differently in between the paramagnetic and antiferromagnetic phases.

We have found that the vertex corrections generally enlarge variations in the ω dependence of optical conductivity. It is also general that the ω-integrated value of the correction is positive, and this is consistent with our expectation. This is because forward scattering processes in quasiparticle damping are not effective for current dissipation, and the vertex corrections compensate their contributions. This also means that the energy gain due to the electron kinetic term is enhanced.

Most importantly, the vertex corrections enhance the Drude peak and its peak shape becomes noticeably sharper. This effect also takes place about the high-energy peak around $\omega \sim U$, and the broad incoherent peak also becomes noticeably sharper. More precisely speaking, the part including the vertex corrections provides a positive contribution around $\omega = 0$ and $\sim U$, while a negative contribution around $\omega \sim 2$. These contributions sharpen the double peak structure in the ω dependence of conductivity. The positive contribution around $\omega = 0$ is gradually suppressed with approaching T_N.

We have found the enhancement of ω-dependent structures also in the antiferromagnetic phase. Most notably this time, the vertex corrections strongly suppress conductivity around $\omega = 0$, and deepen the dip there. The low-energy peak around $\omega \sim 1$ is sharply enhanced instead. [See also the data in Fig. 7(c) at the lower temperature $T = 0.30$.] The peak intensity is enhanced and its width is reduced considerably. This peak comes from motion of low-energy quasiparticles in the gapped bands, and this behavior indicates that the vertex corrections strongly affect their dynamics. The effects in the region of $\omega > 2$ are similar to those in the paramagnetic phase. The corrections sharpen the high-ω peak and deepen the valley.

Thus the most striking feature of the vertex corrections is their opposite effect in the low-ω region depending on temperature. The correction to σ value is positive at high temperatures and negative at low temperatures, and this sign change occurs near T_N. This behavior was already found in $\sigma_{\rm dc}(T)$ in the previous section, but the ω dependence exhibits this change more clearly.

An interesting behavior appears in the paramagnetic phase near T_N. With lowering T, as discussed in the previous section, $\sigma_{\rm dc}(T)$ including the vertex corrections starts decreasing at $T \sim 0.40$, quite higher than T_N. This is due to antiferromagnetic fluctuations strongly enhanced near the transition point. However, in this temperature region, $\sigma(\omega)$ retains a Drude peak and the system remains metallic in this sense. This continues down to $T \sim 0.36$, which is close to the temperature of $\sigma_{0,\rm dc}$ maximum. It is interesting that the temperature and ω dependences of conductivity thus behave differently due to the vertex corrections in this temperature region.

Next, we shall examine the effects of antiferromagnetic fluctuations in more detail. To this end, we separate the vertex correction term in the current correlation function into two parts, $\chi_{\rm vc} = \chi_{\rm vc}^{\rm para} + \chi_{\rm vc}^{\rm mag}$. The RHS of Eq. (6) is a sum of products of four G's, and each G is represented by nonmagnetic g, $\tilde{g}$, and magnetic Δ depending on sublattice index as shown in Eq. (10). The paramagnetic part $\chi_{\rm vc}^{\rm para}$ is the sum of the products that do not contain Δ, while the magnetic part $\chi_{\rm vc}^{\rm mag}$ is the sum of all the others. Namely, $\chi_{\rm vc}^{\rm mag}$ is the part including at least one spin-dependent single-electron Green's function among four double lines in the second diagram in Fig. 1(a).

Figure 6 shows the paramagnetic and magnetic parts of the vertex corrections in current correlation function at various T's. The data are plotted as a function of Matsubara frequency. The magnetic part $\chi_{\rm vc}^{\rm mag}$ is finite only in the antiferromagnetic phase by its definition, whereas the paramagnetic part $\chi_{\rm vc}^{\rm para}$ is sizable in the paramagnetic phase. It is remarkable that the two parts behave opposite to each other in the temperature dependence. The magnetic part grows very rapidly with lowering temperature. In contrast, the paramagnetic part decreases slowly but steadily. Another difference is about their dependence on Matsubara frequency. The maximum of the ${\rm Re}\chi_{\rm vc}^{\rm para}$ stays at $\nu_n = 0$ at all T's. The magnetic part $\chi_{\rm vc}^{\rm mag}$ has a maximum at a finite Matsubara frequency and its position slowly increases with lowering T. It is plausible to expect that this peak is related to deepening of the conductivity dip at $\omega = 0$, and we check this by analytic continuation to real frequency ω.

In Fig. 7, $\sigma_0 + \sigma_{\rm vc}^{\rm para}$ is the optical conductivity calculated from the partial sum $\chi_0 + \chi_{\rm vc}^{\rm para}$, and it is compared with the full conductivity and also the value with no vertex corrections.

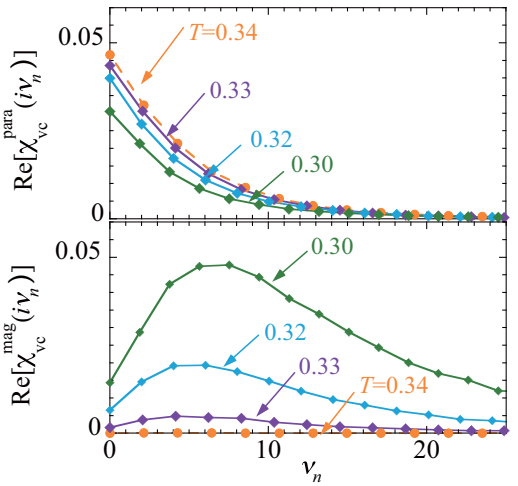

FIG. 6. Contributions of the paramagnetic and magnetic parts of the vertex corrections to current correlation function. Shown is the dependence on Matsubara frequency $\nu_n = 2\pi nT$.

There are two important points. The first point is that the magnetic part dominates in the vertex corrections at low temperature $T = 0.32$, although the two parts have a similar size at this temperature in Fig. 6. The second point is that the magnetic part changes $\sigma(\omega)$ over a much wider range of ω, compared with the paramagnetic part. The change due to the paramagnetic part is limited to around $\omega \sim U$ and $\omega \sim 0$, and the change around $\omega \sim 0$ becomes small at lower

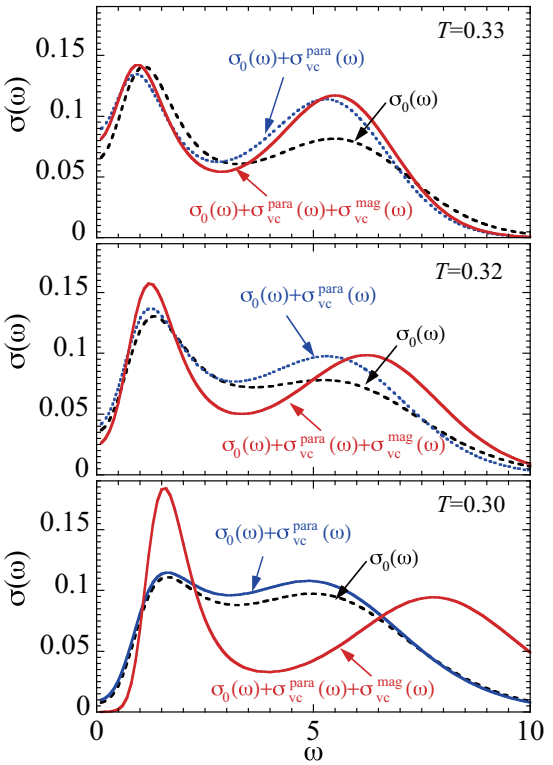

FIG. 7. Effects of the paramagnetic and magnetic parts of the vertex corrections to optical conductivity. The red curves are the full conductivity $\sigma(\omega)$.

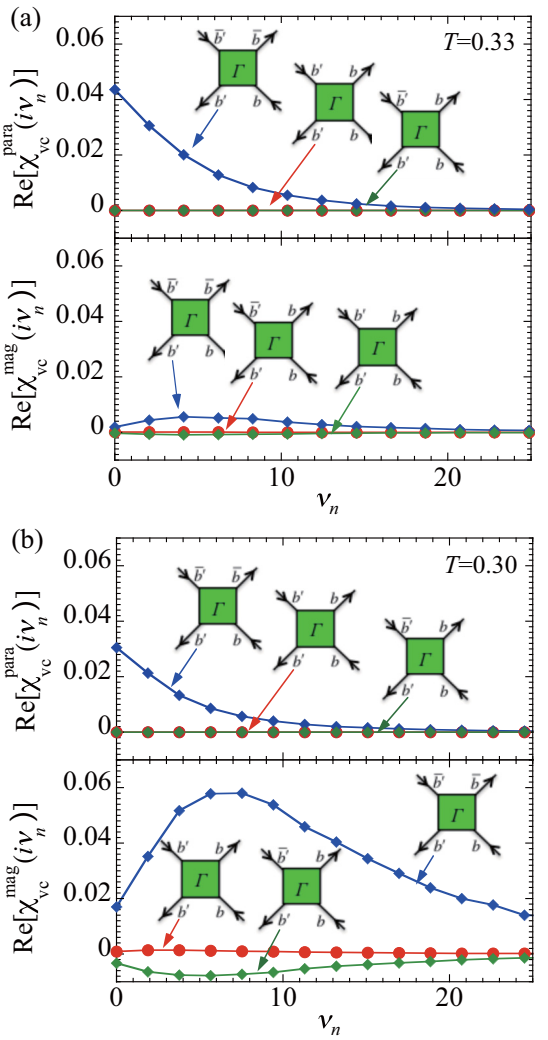

FIG. 8. Comparison of partial Γ sums for $\chi_{\rm vc}(i\nu_n)$. Corresponding to four sublattice indices, 16 elements of Γ's are categorized to the three classes shown. Partial sum is taken in Eq. (6) for each category. Upper and lower panels show the paramagnetic and magnetic parts of the vertex corrections. Temperature is (a) $T = 0.33$ and (b) 0.32.

temperatures. In addition to these two regions, the magnetic part also enhances the peak around $\omega \sim 1$ and deepens the valley between the two peaks.

We now analyze the vertex corrections from a different viewpoint. For the full vertex function Γ, a pair of particle and hole comes in from external lines and they are scattered to another particle-hole pair. In the antiferromagnetic phase, particles and holes have also sublattice degrees of freedom, and it is interesting to examine which combination dominates vertex corrections. Corresponding to the four vertices $b_4 b_1 b_2 b_3$ of Γ in Fig. 1(b), there are 16 combinations and we group them into three categories. Their contributions in $\chi_{\rm vc}^{\rm para}$ and $\chi_{\rm vc}^{\rm mag}$ are shown in Fig. 8. The first category is the ones in which a particle and a hole are on the same sublattice on both incoming and outgoing sides ($b_4 = b_1$, $b_2 = b_3$, plotted with red color). The second category is the ones in which they are on the opposite sublattices on either side ($b_4 = \bar{b}_1$, $b_2 = \bar{b}_3$, blue), and the third category is the remaining ones (green). Each plot

shows the sum of the contributions from the corresponding combinations. The most important point is that the contribution of the second category overwhelms the other two in both $\chi_{\rm vc}^{\rm para}$ and $\chi_{\rm vc}^{\rm mag}$, and therefore charge and density polarizations made of particles and holes on the opposite sublattices play a central role in the vertex corrections. It is also interesting that the third category has a contribution with negative sign. However, its amplitude is much smaller than the second category, although the amplitude grows at lower temperatures.

VI. MOMENTUM DEPENDENCE OF VERTEX FUNCTION

The analysis in the previous section reveals that the most important vertex corrections are about the scattering processes in which a particle and a hole are on the different sublattices to each other both in the initial and final states. In this section, we will analyze how this process depends on the momentum of particle and hole. To this end, we fix the momentum of incoming particle and hole at some characteristic $\mathbf{k}$ points and examine how they are scattered in the Brillouin zone.

The square lattice Hubbard model has a Fermi surface with rotated square shape at half filling, and this is shown in Fig. 1(c). It has been well known that the coherence of quasiparticles on the Fermi surface strongly depends on their position on the surface. The functional renormalization-group study [54,55] or the CDMFT study [21–23] showed that quasiparticles near $(\pi,0)$ or $(0,\pi)$ in the Brillouin zone are very incoherent, because they are scattered not only by antiferromagnetic spin fluctuations but also by Umklapp processes and their renormalized interactions grow rapidly with lowering temperature. Quasiparticles near $(\pi/2, \pm\pi/2)$ or $(-\pi/2, \pm\pi/2)$ are much less incoherent. The most incoherent two $\mathbf{k}$ points are called *hot spots*, while the least incoherent four are called *cold spots*. In this section, we also use the terms *hot* and *cold* for quasiparticles, if they are at either the hot or cold spots.

Thus hot spots and cold spots are opposite limits on the Fermi surface, and we set the incoming momentum at either of the two. As for frequency, we examine the mode with Matsubara frequency $\nu_n = 0$ as the most characteristic one.

Figure 9 shows the $\mathbf{k}$ dependence of the full vertex function $\Gamma^{s,c}_{\mathbf{k}\mathbf{k}'}(i\nu_n = 0)$ at $T = 0.38$ and 0.36 in the paramagnetic phase. The incoming particle is set at the cold spot $\mathbf{k}' = (\pi/2,\pi/2)$ in (a), while at the hot spot $(\pi,0)$ in (b). The incoming hole is at $-\mathbf{k}'$. Γ^c and Γ^s are the charge and spin vertex defined by

$$\Gamma^c_{\mathbf{k}\mathbf{k}'} \equiv \sum_{\sigma,\sigma'} \Gamma_{\mathbf{k}\sigma\mathbf{k}'\sigma'}, \quad \Gamma^s_{\mathbf{k}\mathbf{k}'} \equiv \sum_{\sigma,\sigma'} \sigma\sigma' \Gamma_{\mathbf{k}\sigma\mathbf{k}'\sigma'}, \qquad (11)$$

where all the Matsubara frequencies are $i\nu_n = 0$. Note that the vertex function Γ does not have sublattice indices in the paramagnetic phase and the details of Γ were explained in our previous work [17]. The data in Fig. 9 provide important information on residual effective interactions between quasiparticles. Note that optical conductivity is the response of charge current and therefore only the charge vertex contributes to $\chi_{\rm vc}$.

First, we examine the difference in the $\mathbf{k}$ dependence between the spin and charge vertices; more specifically, dependence on the momentum difference $\Delta\mathbf{k} \equiv \mathbf{k} - \mathbf{k}'$. The most prominent difference is that forward scatterings are

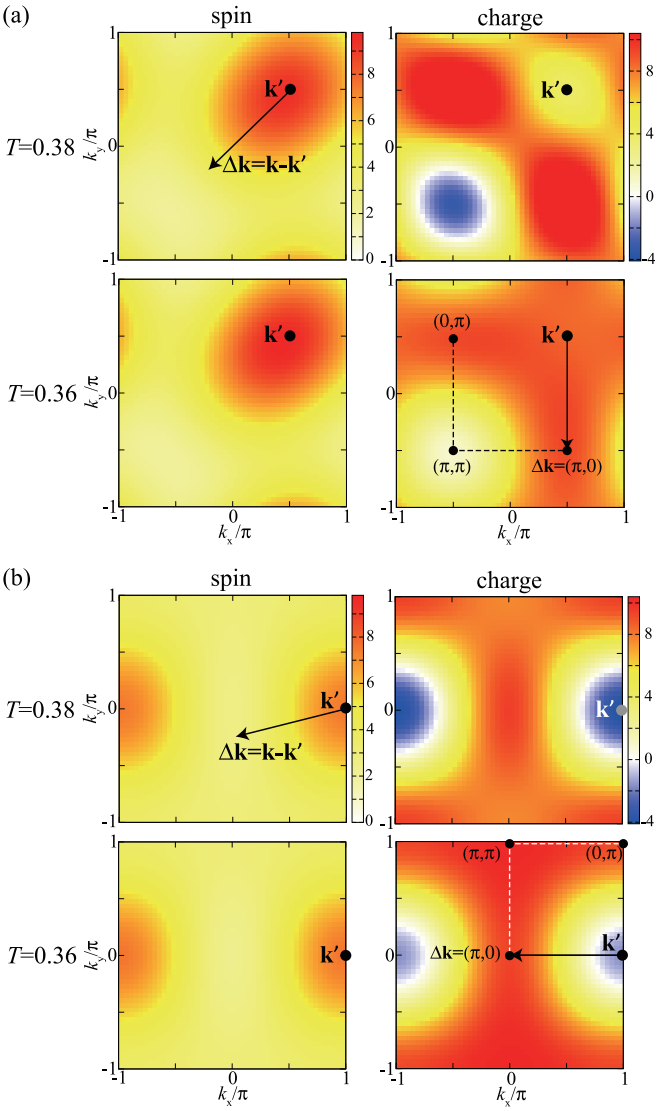

FIG. 9. Momentum dependence of the spin and charge parts of the full vertex function, $\Gamma^{s,c}_{\mathbf{k}\mathbf{k}'}(i\nu_n = 0)$, in Eq. (11). The case of (a) cold quasiparticles $\mathbf{k}' = (\pi/2,\pi/2)$ and (b) hot quasiparticles $\mathbf{k}' = (\pi,0)$. Dotted line is a guide for the path examined in Sec. VI.

dominant and have a positive amplitude in the spin vertex, while they are very weak in the charge vertex. Here, forward scatterings refer to the cases of small $|\Delta\mathbf{k}|$. In the charge vertex, Γ is maximum for $\Delta\mathbf{k} \sim (\pi,0)$ or $(0,\pi)$. (This depends slightly on temperature, and this will be discussed later.) These features are common for both incoming quasiparticles on the cold spot and those on the hot spot. It is also interesting that the forward scatterings have a small negative amplitude in the hot spot case. However, the $\mathbf{k}$ dependence becomes quite weak at lower temperature $T = 0.36$ in the charge vertex.

Secondly, let us compare the behaviors between the cold and hot quasiparticles. As expected, Γ is considerably larger for the hot quasiparticle. An interesting point is that the difference is evident only in the charge vertex, while the difference in the spin vertex is small. One difference in the spin vertex is that Γ is minimum and negative for $\Delta\mathbf{k} \sim (\pi,\pi)$ at the cold spot, while the minimum position is $\Delta\mathbf{k} \sim (\pi,0)$ for the hot spot.

Otherwise, the difference in the **k** dependence is rather weak in the spin vertex.

The difference between cold and hot quasiparticles also appears in the evolution with temperature in the charge vertex. Γ^c decreases at low temperature for the cold quasiparticle and strongly increases for the hot quasiparticle, which is again consistent with the momentum dependence of quasiparticle lifetime.

Another interesting point about the charge vertex is that the **k** points with large Γ^c for the hot quasiparticle distribute very widely in the Brillouin zone at $T = 0.36$ [see the bottom-right panel in Fig. 9(b)]. These points are around the lines (q,π) and $(0,q)$ with $(-\pi \leqslant q \leqslant \pi)$, and the maximum is at $\mathbf{k} = (0, \pm\pi)$. The corresponding momentum difference $\Delta\mathbf{k}$ spans the parts (π,q) and (q,π). They are the momentum region where the charge correlation is found enhanced at low temperatures in the variational MC study [56]. The equal-time charge correlation function has an extended peak along the line between (π,π) and $(\pi,0) = (0,\pi)$ points in the Brillouin zone, and the momentum dependence along the line is suppressed for strong repulsion U. We find the same trend also for the cold quasiparticle [Γ^c in Fig. 9(a)]. With lowering temperature, the variation in Γ^c along the line $\mathbf{k} = (\pi/2, -\pi/2)$-$(-\pi/2, -\pi/2)$-$(-\pi/2,\pi/2)$ (dotted line inside the data) becomes suppressed at $T = 0.36$, and this is common to the behavior of the hot quasiparticle in Fig. 9(b). Despite having found the relation of this behavior with the charge correlation, the behavior of $\Gamma^c_{\mathbf{k},\mathbf{k}'}$ is not well understood yet, and a further study should investigate this point in future.

The full vertex function $\Gamma^{s,c}_{\mathbf{p}\mathbf{p}'}$ in the antiferromagnetic phase is shown in Fig. 10. The data are calculated at $T = 0.33$, which is close to T_N. We define the charge and spin vertices in the same way as before, but one should note that in the antiferromagnetic phase the spin vertex also contributes to $\chi_{\rm vc}$ in the current correlation function. This is because the single-electron Green's functions contain a spin-dependent component Δ, and products of Γ^s and some Δ's contribute to $\chi_{\rm vc}$. Now, Γ has the sublattice indices and specifically we examine the part that a particle and a hole are on the different sublattices both on the incoming and outgoing sides, since the analysis in the previous section showed that this has the dominant contribution. In the figure, the case that a particle on one sublattice is scattered to a particle on the same sublattice (PP channel) and the case that it is scattered to a hole on the same sublattice (PH channel) are shown separately. Recall that the Brillouin zone is reduced to a half in the antiferromagnetic phase.

First of all, the **p** dependence in the PP and PH channels are very similar to each other, but the amplitude is different. The sign is the same for the case of $\mathbf{p}' = (\pi,0)$, but opposite for $\mathbf{p}' = (\pi/2,\pi/2)$. Generally, the spin vertex has much larger amplitudes in the PH channel, while the charge vertex has larger amplitudes in the PP channel but the difference is smaller than the case of the spin vertex. It is also general that the spin and charge vertices have opposite sign for the global phase of Γ.

It is very important that the dependence on $\Delta\mathbf{p} \equiv \mathbf{p} - \mathbf{p}'$ is very different between the two $\mathbf{p}'$ cases, and this is true for both spin and charge vertices. This feature is distinct from that in the paramagnetic phase.

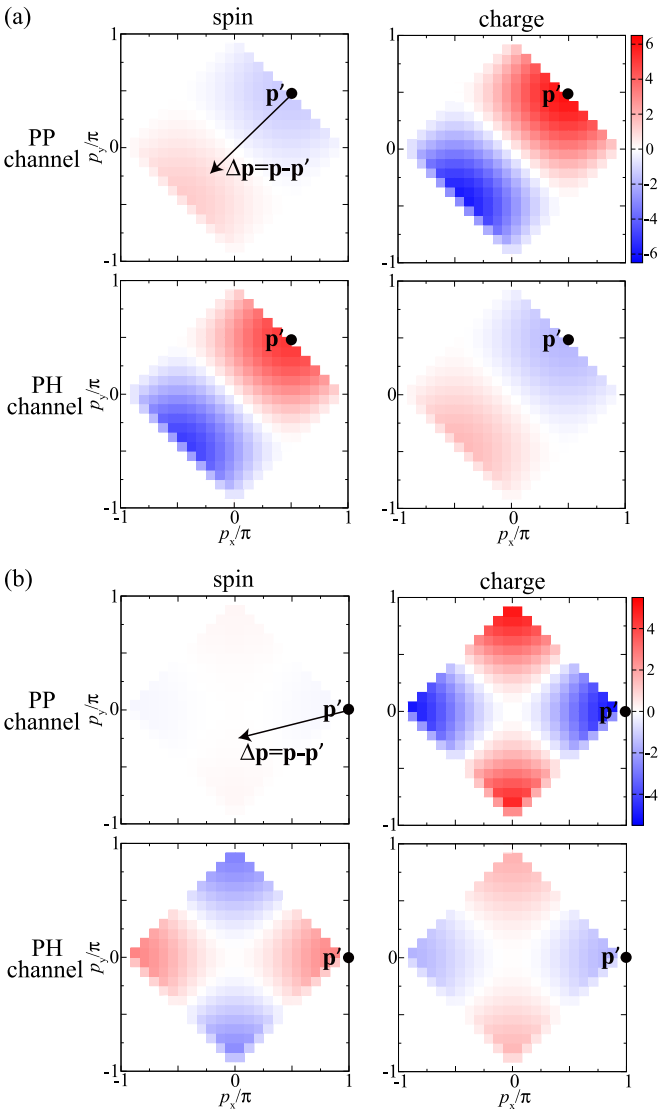

FIG. 10. Spin vertex $\sum_{\sigma\sigma'} \sigma\sigma' \Gamma^{b\bar{b}b'\bar{b}'}_{\mathbf{p}\sigma\mathbf{p}'\sigma'}(i\nu_n = 0)$ (left column) and charge vertex $\sum_{\sigma\sigma'} \Gamma^{b\bar{b}b'\bar{b}'}_{\mathbf{p}\sigma\mathbf{p}'\sigma'}(i\nu_n = 0)$ (right column) at $T = 0.33$. The case of (a) $\mathbf{p}' = (\pi/2,\pi/2)$ and (b) $\mathbf{p}' = (\pi,0)$. In each case, the particle-particle (PP) channel $(b\bar{b}b'\bar{b}')$ = (ABAB) and (BABA) is shown in the first row, and the particle-hole (PH) channel $(b\bar{b}b'\bar{b}')$ = (ABBA) and (BAAB) is shown in the second row.

We examine the momentum dependence of Γ in more detail. For $\mathbf{p}' = (\pi/2,\pi/2)$, the momentum dependence is mainly dominated by $\Delta p_x + \Delta p_y$ with much smaller dependence on $\Delta p_x - \Delta p_y$. This is similar to the dependence of Γ^c for the cold quasiparticle in the paramagnetic phase. However, the dependence is much more one dimensional now and the direction perpendicular to the initial wave vector $\mathbf{p}'$ provides only small correction.

The dependence is quite different for $\mathbf{p}' = (\pi,0)$. In the reduced Brillouin zone, the sign of Γ is determined by $\pm\cos[\frac{1}{2}(\Delta p_x + \Delta p_y)]\cos[\frac{1}{2}(\Delta p_x - \Delta p_y)] \propto \pm(\cos\Delta p_x + \cos\Delta p_y)$, where the sign depends on the spin or charge part of the vertex. This momentum dependence is the one of nearest-neighbor interactions in real space, and this result indicates that nearest-neighbor correlations are

dominant for the vertex corrections of those quasiparticles near $(\pi,0)$.

VII. DISCUSSIONS AND SUMMARY

In this paper, we have studied optical conductivity near the antiferromagnetic transition in a square-lattice Hubbard model at half filling. To calculate optical conductivity, we have used a cluster dynamical mean-field approach for obtaining single- and two-electron Green's functions. For taking account of electron correlation effects, we have derived a new formula of the vertex corrections in the antiferromagnetic phase based on our previous one for the paramagnetic phase. The derived formula of the vertex corrections is easily generalized for other response functions including Raman spectrum. We have found that the vertex corrections change various important details in temperature and frequency dependence of conductivity near the antiferromagnetic transition. This point differs from our previous study on optical conductivity near the Mott transition in a frustrated triangular lattice.

An important effect of the vertex corrections is that they enhance variations in frequency dependence of conductivity: the Drude peak in the paramagnetic phase is enhanced and the broad incoherent peak related to the Hubbard band is sharpened. The valley in the frequency dependence between these two peaks is deepened. Optical conductivity shows a dip at $\omega = 0$ in the antiferromagnetic phase, and the vertex corrections also enhance this dip.

Another important finding is about a temperature region just above the antiferromagnetic transition temperature. In this region, dc conductivity decreases with lowering temperature, which is similar to a pseudogap phase [57], but no indication of pseudogap is found in the single-electron spectrum and the optical conductivity. One needs care about the presence of pseudogap. A recent quantum Monte Carlo study reported a pseudogap behavior for weak to intermediate Coulomb repulsion in the square-lattice Hubbard model at half filling [58]. However, since its observed characteristic temperature is lower than the antiferromagnetic transition temperature in the present work, therefore this is not a controversy. It is noticeable that this temperature region is expanded in the result with the vertex correction included, and this unusual metal behavior is strengthened by the vertex correction. There has been only few experimental studies on electric conductivity in quasi-two-dimensional antiferromagnets with an integer electron density, and in most of the materials the temperature dependence is insulating in the whole temperature range. One interesting exception is the layered organic compound, β'-type $Pd(dmit)_2$ compound [59,60]. The electric conductivity in β'-type $Pd(dmit)_2Me_4P$ is metallic at high temperature, but turns to insulating at around 200 K at ambient pressure, while the antiferromagnetic transition temperature is $T_N \sim 40$ K. Unfortunately, this material is not an ideal realization of the square-lattice Hubbard model due to moderate frustration, but the antiferromagnetic transition takes place. It is interesting to examine if there exists an evidence of pseudogap or not above T_N.

For better understanding of the vertex corrections, we have analyzed which types of fluctuations are important in the formula. The formula shows that the vertex corrections are determined by the vertex function and four single-electron Green's functions. Concerning the part of the Green's functions, their spin dependent components provide a dominant contribution in the antiferromagnetic phase. Some of them couple with the spin part of the vertex function, while some of the others couple with the charge part, and both contribute to conductivity. Concerning the part of the vertex function, a predominant contribution is given by the scattering processes of polarization made of a particle on one sublattice and a hole on the other sublattice.

We have also studied the momentum dependence of the vertex function. We have found that the momentum dependence differs significantly in the paramagnetic phase between the charge vertex and the spin vertex. An important point is that for quasiparticles near $(\pi,0)$ or $(0,\pi)$ in the Brillouin zone the vertex functions are strongly enhanced near the antiferromagnetic instability and the dependence on the scattered momentum indicates the importance of Umklapp scatterings. In the antiferromagnetic phase, the charge vertex and spin vertex functions have a similar momentum dependence but the sign is opposite. The antiferromagnetic phase also has very different momentum dependence of the vertex function between quasiparticles at different positions in the Brillouin zone. For those at $(\pi,0)$ or $(0,\pi)$, the momentum dependence is dominated by nearest-neighbor correlations. For those at $(\pi/2, \pm\pi/2)$, the momentum dependence is quite one dimensional. At this moment, it is not clear yet how these exotic correlations affect conductivity, but we believe that these detailed data in the vertex function and the vertex corrections obtained in the present work will provide useful information in future for constructing theories for better understanding of conductivity in the Hubbard model.

ACKNOWLEDGMENTS

The authors are grateful to Kazumasa Hattori for valuable discussions and his useful comments. Numerical computations have been performed with using the facilities at Supercomputer Center in ISSP and Information Technology Center, both of which are at the University of Tokyo, as well as the RIKEN Integrated Cluster of Clusters (RICC) facility. This work has been supported by a Grant-in-Aid for Scientific Research from the Japan Society for the Promotion of Science (Grant No. 25400359).

[1] A. Georges, G. Kotliar, W. Krauth, and M. Rozenberg, Rev. Mod. Phys. **68**, 13 (1996).

[2] M. H. Hettler, M. Mukherjee, M. Jarrell, and H. R. Krishnamurthy, Phys. Rev. B **61**, 12739 (2000).

[3] G. Kotliar, S. Y. Savrasov, G. Pálsson, and G. Biroli, Phys. Rev. Lett. **87**, 186401 (2001).

[4] O. Parcollet, G. Biroli, and G. Kotliar, Phys. Rev. Lett. **92**, 226402 (2004).

[5] B. Kyung and A.-M. S. Tremblay, Phys. Rev. Lett. **97**, 046402 (2006).

[6] T. Ohashi, N. Kawakami, and H. Tsunetsugu, Phys. Rev. Lett. **97**, 066401 (2006).

[7] Y. Z. Zhang and M. Imada, Phys. Rev. B **76**, 045108 (2007).

[8] B. Kyung, Phys. Rev. B **75**, 033102 (2007).

[9] H. Park, K. Haule, and G. Kotliar, Phys. Rev. Lett. **101**, 186403 (2008).

[10] E. Gull, P. Werner, X. Wang, M. Troyer, and A. J. Millis, Eur. Phys. Lett. **84**, 37009 (2008).

[11] T. Ohashi, T. Momoi, H. Tsunetsugu, and N. Kawakami, Phys. Rev. Lett. **100**, 076402 (2008).

[12] A. Liebsch, H. Ishida, and J. Merino, Phys. Rev. B **79**, 195108 (2009).

[13] D. Galanakis, T. D. Stanescu, and P. Phillips, Phys. Rev. B **79**, 115116 (2009).

[14] Y. Furukawa, T. Ohashi, Y. Koyama, and N. Kawakami, Phys. Rev. B **82**, 161101(R) (2010).

[15] G. Kotliar, E. Lange, and M. J. Rozenberg, Phys. Rev. Lett. **84**, 5180 (2000).

[16] P. Sémon and A.-M. S. Tremblay, Phys. Rev. B **85**, 201101(R) (2012).

[17] T. Sato, K. Hattori, and H. Tsunetsugu, Phys. Rev. B **86**, 235137 (2012).

[18] A. Macridin, M. Jarrell, T. Maier, P. R. C. Kent, and E. D'Azevedo, Phys. Rev. Lett. **97**, 036401 (2006).

[19] M. Ferrero, P. S. Cornaglia, L. De Leo, O. Parcollet, G. Kotliar, and A. Georges, Phys. Rev. B **80**, 064501 (2009).

[20] P. Werner, E. Gull, O. Parcollet, and A. J. Millis, Phys. Rev. B **80**, 045120 (2009).

[21] M. Civelli, M. Capone, S. S. Kancharla, O. Parcollet, and G. Kotliar, Phys. Rev. Lett. **95**, 106402 (2005).

[22] T. D. Stanescu and G. Kotliar, Phys. Rev. B **74**, 125110 (2006).

[23] B. Kyung, S. S. Kancharla, D. Sénéchal, A.-M. S. Tremblay, M. Civelli, and G. Kotliar, Phys. Rev. B **73**, 165114 (2006).

[24] A. Liebsch and N.-H. Tong, Phys. Rev. B **80**, 165126 (2009).

[25] S. Sakai, Y. Motome, and M. Imada, Phys. Rev. Lett. **102**, 056404 (2009).

[26] S. Sakai, Y. Motome, and M. Imada, Phys. Rev. B **82**, 134505 (2010).

[27] G. Sordi, P. Sémon, K. Haule, and A.-M. S. Tremblay, Phys. Rev. Lett. **108**, 216401 (2012).

[28] J. Merino and O. Gunnarsson, Phys. Rev. B **89**, 245130 (2014).

[29] M. J. Rozenberg, G. Kotliar, H. Kajueter, G. A. Thomas, D. H. Rapkine, J. M. Honig, and P. Metcalf, Phys. Rev. Lett. **75**, 105 (1995).

[30] J. Merino and R. H. McKenzie, Phys. Rev. B **61**, 7996 (2000).

[31] V. S. Oudovenko, G. Pálsson, S. Y. Savrasov, K. Haule, and G. Kotliar, Phys. Rev. B **70**, 125112 (2004).

[32] T. Mutou and H. Kontani, Phys. Rev. B **74**, 115107 (2006).

[33] D. J. García, E. Miranda, K. Hallberg, and M. J. Rozenberg, Phys. Rev. B **75**, 121102(R) (2007).

[34] J. Merino, M. Dumm, N. Drichko, M. Dressel, and R. H. McKenzie, Phys. Rev. Lett. **100**, 086404 (2008).

[35] F. Lu, W.-H. Wang, and L.-J. Zou, Phys. Rev. B **77**, 125117 (2008).

[36] S. Chakraborty, D. Galanakis, and P. Phillips, Phys. Rev. B **78**, 212504 (2008).

[37] N. Lin, E. Gull, and A. J. Millis, Phys. Rev. B **82**, 045104 (2010).

[38] S. Okamoto, D. Sénéchal, M. Civelli, and A.-M. S. Tremblay, Phys. Rev. B **82**, 180511(R) (2010). Note that they calculated optical conductivity by using both the CDMFT and DCA.

[39] N. Lin, E. Gull, and A. J. Millis, Phys. Rev. B **80**, 161105(R) (2009).

[40] P. Werner, A. Comanac, L. de Medici, M. Troyer, and A. J. Millis, Phys. Rev. Lett. **97**, 076405 (2006).

[41] In this paper, we use the following notation for imaginary-time operators: $c(\tau) = e^{\tau H} c\, e^{-\tau H}$ and $c^\dagger(\tau) = e^{\tau H} c^\dagger e^{-\tau H}$. Therefore, $c^\dagger(\tau) \neq [c(\tau)]^\dagger$.

[42] P. R. C. Kent, M. Jarrell, T. A. Maier, and Th. Pruschke, Phys. Rev. B **72**, 060411 (2005).

[43] N. D. Mermin and H. Wagner, Phys. Rev. Lett. **17**, 1133 (1966).

[44] M. Jarrell and J. E. Gubernatis, Phys. Rep. **269**, 133 (1996).

[45] R. Kubo, J. Phys. Soc. Jpn. **12**, 570 (1957).

[46] P. Nozières, *Theory of Interacting Fermi Systems* (Addison-Wesley, Redwood City, CA, 1964).

[47] H. Kusunose, J. Phys. Soc. Jpn. **75**, 054713 (2006).

[48] A. Toschi, A. A. Katanin, and K. Held, Phys. Rev. B **75**, 045118 (2007).

[49] A. A. Abrikosov and V. M. Genkin, Zh. Eksp. Teor. Fiz. **65**, 842 (1973) [Sov. Phys. JETP **38**, 417 (1974)].

[50] M. V. Klein and S. B. Dierker, Phys. Rev. B **29**, 4976 (1984).

[51] T. P. Devereaux and A. P. Kampf, Phys. Rev. B **59**, 6411 (1999).

[52] Note that the local excitation spectrum can also be calculated directly from the cluster Green's function, $A^A_{\mathrm{cl},\sigma}(\omega) = -\frac{1}{2\pi}\mathrm{Im}\sum_{j\in A} G^{jj}_\sigma(\omega + i0)$. The momentum average A^A_σ calculated from the cumulant method agrees with this value well. The relative error is very small and at most less than 0.8% in the data in Fig. 3(a). This is an evidence that the cumulant method works well for periodization of the Green's function.

[53] P. Fazekas, *Lecture Notes on Electron Correlation and Magnetism* (World Scientific, Singapore, 1999) and reference therein.

[54] C. Honerkamp, M. Salmhofer, N. Furukawa, and T. M. Rice, Phys. Rev. B **63**, 035109 (2001).

[55] P. Kopietz, L. Bartosch, and F. Schütz, *Introduction to the Functional Renormalization Group* (Springer, New York, 2010), and references therein.

[56] H. Otsuka, J. Phys. Soc. Jpn. **61**, 1645 (1992).

[57] M. Imada, A. Fujimori, and Y. Tokura, Rev. Mod. Phys. **70**, 1039 (1998).

[58] D. Rost, E. V. Gorelik, F. Assaad, and N. Blümer, Phys. Rev. B **86**, 155109 (2012).

[59] K. Kanoda and R. Kato, Annu. Rev. Condens. Matter Phys. **2**, 167 (2011).

[60] R. Kato, Y.-L. Liu, Y. Hosokoshi, S. Aonuma, and H. Sawa, Mol. Cryst. Liq. Cryst. **296**, 217 (1997).